Supplementary Materials for

Autonomous Multi-Robot Synthesis and Optimization of Metal Halide Perovskite Nanocrystals

Jinge Xu[1], Christopher H.J. Moran[1], Arup Ghorai[1], Fazel Bateni[1], Jeffery A. Bennett[1], Nikolai Mukhin[1], Koray Latif[2], Andrew Cahn[3], Pragyan Jha[1], Fernando Delgado Licona[1], Sina Sadeghi[1], Lior Politi[1], and Milad Abolhasani[1]*

[1] *Department of Chemical and Biomolecular Engineering, North Carolina State University, Raleigh, NC 27695 USA*

[2] *Department of Computer Science, North Carolina State University, Raleigh, NC 27695 USA*

[3] *Department of Mechanical and Aerospace Engineering, North Carolina State University, Raleigh, NC 27695 USA*

E-mail: abolhasani@ncsu.edu

Data preprocessing

Following the data acquisition from the characterization robot, UV-Vis absorption spectra of the reaction solvent (o-xylene, reference) and automatically synthesized MHP NCs (samples) as well as the emission spectra of MHP NCs are collected and saved to a specific folder of the specific experimental iteration corresponding to the target peak emission energy (E_P) campaign. A custom-developed Python script then automatically processes the acquired spectral data to extract the optical features of interest (i.e., output parameters), including E_P, proxy photoluminescence quantum yield (P_{PLQY}), and emission linewidth (full-width-at-half-maximum, FWHM). The processed data with the corresponding input parameters are then stored in a single .csv file ready for the SDL artificial intelligence (AI) agent to update its surrogate model and suggest a new set of synthesis conditions to be automatically tested by the SDL hardware. Considering four replicates of each NC synthesis condition, the medians of the optical properties from the four replicates are utilized as the representative values.

Calculation of absorbance value at excitation (abs@excitation)

Subtract the reference solvent absorption spectra from the NC absorption; then, identify the wavelength closest to the 365 nm, the excitation wavelength for emission spectra measurement; then, obtain the absorbance value at that wavelength as the absorbance at excitation wavelength.

$$\text{net absorbance} = \text{NC absorbance} - \text{reference absorbance} \quad (Eq.S1)$$

$$i = \text{argmin}(\text{absorbance wavelength} - 365) \quad (Eq.S2)$$

$$\text{abs@excitation} = \text{net absorbance}[i] \quad (Eq.S3)$$

Calculation of E_P

Identify the wavelength with the maximum emission intensity, convert the wavelength to energy.

$$j = \text{argmax(emission intensity)} \quad (Eq.S4)$$
$$\lambda = \text{emission wavelength}[j]\ (\text{nm}) \quad (Eq.S5)$$
$$E_{\text{P}} = \frac{1239.8}{\lambda}\ (\text{eV}) \quad (Eq.S6)$$

Calculation of P_{PLQY}

Calculate the integral of the NC emission spectra over the emission wavelength as the emitted photon, calculate the P_{PLQY} by dividing the integral by abs@excitation.

$$P_{\text{PLQY}} = \frac{\int \text{emission}}{\text{abs@excitation}} \quad (Eq.S7)$$

Calculation of FWHM

Identify the emission energy (smaller than E_P) with half of the maximum emission intensity, then identify the emission energy (larger than E_P) with half of the maximum emission intensity, calculate the difference between the two identified emission energies as the FWHM.

$$j = \text{argmax(emission intensity)} \quad (Eq.S8)$$
$$k_1 = \text{argmin}\left(\text{emission intensity} - \frac{1}{2}\max\{\text{emission intensity}\}\right), k_1 < j \quad (Eq.S9)$$
$$k_2 = \text{argmin}\left(\text{emission intensity} - \frac{1}{2}\max\{\text{emission intensity}\}\right), k_2 > j \quad (Eq.S10)$$

$$\lambda_1 = \text{emission wavelength}\ [k_1]\ (\text{nm}) \quad (Eq.S11)$$
$$\lambda_2 = \text{emission wavelength}\ [k_2]\ (\text{nm}) \quad (Eq.S12)$$
$$E_1 = \frac{1239.8}{\lambda_1}\ (\text{eV}) \quad (Eq.S13)$$
$$E_2 = \frac{1239.8}{\lambda_2}\ (\text{eV}) \quad (Eq.S14)$$
$$\text{FWHM} = E_1 - E_2 \quad (Eq.S15)$$

Rainbow's AI agent: Automated decision-making algorithm

Rainbow's AI agent uses a constrained, mixed-variable, multi-objective Bayesian optimization (BO) algorithm to automatically suggest the new experimental conditions (see Fig. 4) in the main text). The input parameters are the choice of organic acid (discrete variable) and concentration of precursors (continuous variables), including Cs, Pb, DDAB, organic acid, and halide precursors.

The output parameters include E_P, P_{PLQY}, and FWHM. The dataset is normalized between [0,1] for model training and prediction. The parameter space boundaries are reported in Tables S1 and S2. The AI agent's BO algorithm utilizes a surrogate model trained with normalized experimental conditions (inputs) and measured NC properties (outputs) to map the ligand structure-synthesis-properties relationship of MHP NCs. An acquisition function is selected as the metric function evaluating the input candidates and output the acquisition score. Then, points sampled from the parameter space are optimized and converged to global optimum according to the acquisition function. The 24 candidates with the top 24 acquisition scores are recorded as the experimental conditions that are predicted to mostly enlarge the Pareto-Front.

Surrogate model

The surrogate model employed to predict the optical properties (E_P, P_{PLQY}, FWHM) for a given input NC synthesis condition is a Gaussian process regression (GPR) model trained with dataset of only successful data resulting in emissive MHP NCs. In order to handle the mixed-variable input space, the GPR uses a kernel combining the categorical kernel, (based on Hamming distances) and a regular kernel into the form shown in Eq. S16 (*39*):

$$K\big((x_1, c_1), (x_2, c_2)\big) = K_{\mathrm{cont}_1}(x_1, x_2) + K_{\mathrm{cat}_1}(c_1, c_2) + K_{\mathrm{cont}_2}(x_1, x_2) + K_{\mathrm{cat}_2}(c_1, c_2) (Eq. S16)$$

Where x_i and c_i are the continuous and categorical input variables, respectively. The surrogate model is updated with accumulating dataset after each experimental iteration. Given the limited yet costly experimental data, we trained a sparse GPR on all available experimental observations to maximize information capture. Kernel hyperparameters, i.e., length scales, signal variance, and noise level, were determined by maximizing the log marginal likelihood, which embodies Occam's razor by penalizing overly flexible models, thereby eliminating the need for a hold-out validation split. RBF kernel further acts as an implicit Tikhonov regularizer, imposing smoothness constraints that mitigate overfitting. Collectively, this Bayesian framework ensures that the surrogate accurately captures the nonlinear relationships between synthesis parameters and nanocrystal properties while maintaining strong predictive reliability.

Classifier model

The classifier model used to predict the probability of emissive synthesis (P_{emissive}, where $P_{\text{emissive}} \in [0,1]$) for a given input condition is a GPR model trained with the entire dataset, including both emissive (labeled 1) and non-emissive (labeled 0) synthesis data. The classifier model is updated with accumulating dataset after each experimental iteration.

Objectives

The desired target for each output parameter is a user-defined value of the E_P along with the highest P_{PLQY} and the lowest FWHM possible for the targeted E_P. To facilitate the hypervolume calculation of E_P, P_{PLQY} and FWHM during the multi-objective optimization process, the desired target of each output is expected to be at the maximum (normalized value 1), the features are transformed to specific functions:

Objective 1 (minimize the distance to the target E_P):

$$\max \{\text{Res} - |\text{predicted } E_P - \text{target } E_P|, 0\} \times P_{\text{emissive}}$$

where Res denotes as the acceptable deviation from the target E_P value, Res = 2%×target E_P

Objective 2 (maximize the P_{PLQY}): predicted P_{PLQY}

Objective 3 (minimize FWHM): 1 – predicted FWHM

The actual objective function is a tensor stacking objectives 1-3.

Hypervolume calculation

The optical properties, including the E_P, P_{PLQY}, and FWHM, are normalized to [0,1] using the boundaries provided in Table S2. The 3-dimensional hypervolume is calculated using the default hypervolume calculation function in BoTorch, where the boundary point [0,0,0] is selected as the reference point to ensure all the points possess positive hypervolume and facilitate the hypervolume calculation.

Acquisition function Rainbow's AI agent utilizes a specific decision-making policy for multi-objective BO, called noisy expected hypervolume improvement (NEHVI), which is a one-step Bayes-optimal policy for maximizing the hypervolume dominated by the Pareto-Front in noisy and noisy-free settings (*40*).

Optimization

512 random initial set of input points are generated by Sobol Sampling and optimized individually *via* sequential least squares programming optimization method. The optimized point with highest acquisition score is selected as the first candidate condition to be tested by the Rainbow hardware. Appending the first candidate with its predicted optical properties to the current belief (surrogate model), the AI agent redoes partitioning and optimization step, generating the next candidate condition. The AI agent continues the partitioning and optimization process until 24 suitable synthesis candidate conditions are generated. The surrogate model and classifier model remain unchanged during the candidate generation process.

Rainbow's robotic components

To facilitate the replenishment of the pipetting robot's consumables, we designed and employed two motorized hoppers, henceforth referred to as 'plate feeders' (Fig. S3). Unlike the other experimental modules of the Rainbow workflow, each of these feeders operated independently from the central process automation module by virtue of having its own dedicated microcontroller. The principal motivating factor for these feeders was to minimize the number of robotic arm positions and movements that would otherwise have had to be encoded. During each full operation cycle of the Rainbow's workflow (up to 150 min), one pipette tip rack and two well plates were utilized. Thus, 12 well plates and 6 pipette tip racks allow for 15 h of continuous, uninterrupted operation of Rainbow.

The plate feeders were constructed from a mixture of custom-designed 3D-printed parts and commercial off-the-shelf components. From a mechanical standpoint, each plate feeder had at its core, a commercially-sourced ball screw linear actuator driven by a NEMA 23 stepper motor. Custom-designed, modular 3D-printed labware racks were affixed to the sliding block of the linear actuators, forming a single combined labware shelf that the linear actuator would move up and down as needed. Each linear actuator was controlled by an Arduino Due microcontroller unit (MCU) connected to a DM542T stepper motor driver, with both modules being housed outside the enclosure in a control box. The custom code running on the MCUs was written using Arduino IDE using the default programming language thereof.

Each labware feeder could operate in one of two modes: a normal mode, or a reloading mode. It is worth noting that, out of safety considerations stemming from a potential pinch hazard posed by the moving racks, changing between modes had to be done manually by the operator via a switch on the control panel. When reloading mode is enabled by the operator, the linear actuator moves the feeder's rack down until a floor sensor is triggered, whereupon all movement stops, thereby allowing the operator to safely restock the feeder with labware. Upon being switched back into normal mode by the operator, the rack will slowly be moved up until the labware sensor, a limit switch marking a fixed position in space, is activated by a plate or pipette tip rack touching it, after which the feeder will halt. Upon removal of a piece of labware by the robotic arm, the sensor will no longer be in a closed state, which triggers a countdown of 1 minute to give the robotic arm time to move clear of the plate feeder. After this countdown, the feeder will resume upward motion until the labware sensor is again activated, or the ceiling sensor is instead tripped by the linear actuator reaching the end of its travel—a state that corresponds to an empty rack. When the ceiling sensor is activated, a red LED will flash on the control panel to notify the operator that the feeder is empty.

The multimode plate reader (BioTek Cytation 5, Agilent) was controlled programmatically via Agilent's Gen5 OLE Automation interface. A custom C# wrapper accessed this interface to configure optical settings (absorbance wavelength, excitation/emission pairs, integration time) and to trigger data acquisition. The wrapper was invoked asynchronously by the master Python scheduler, enabling seamless hand-off between synthesis and characterization tasks. Spectra were exported automatically as CSV files, parsed in Python, and routed to the BO loop, thereby maintaining closed-loop autonomy across the entire experimental cycle.

Fig. S1.

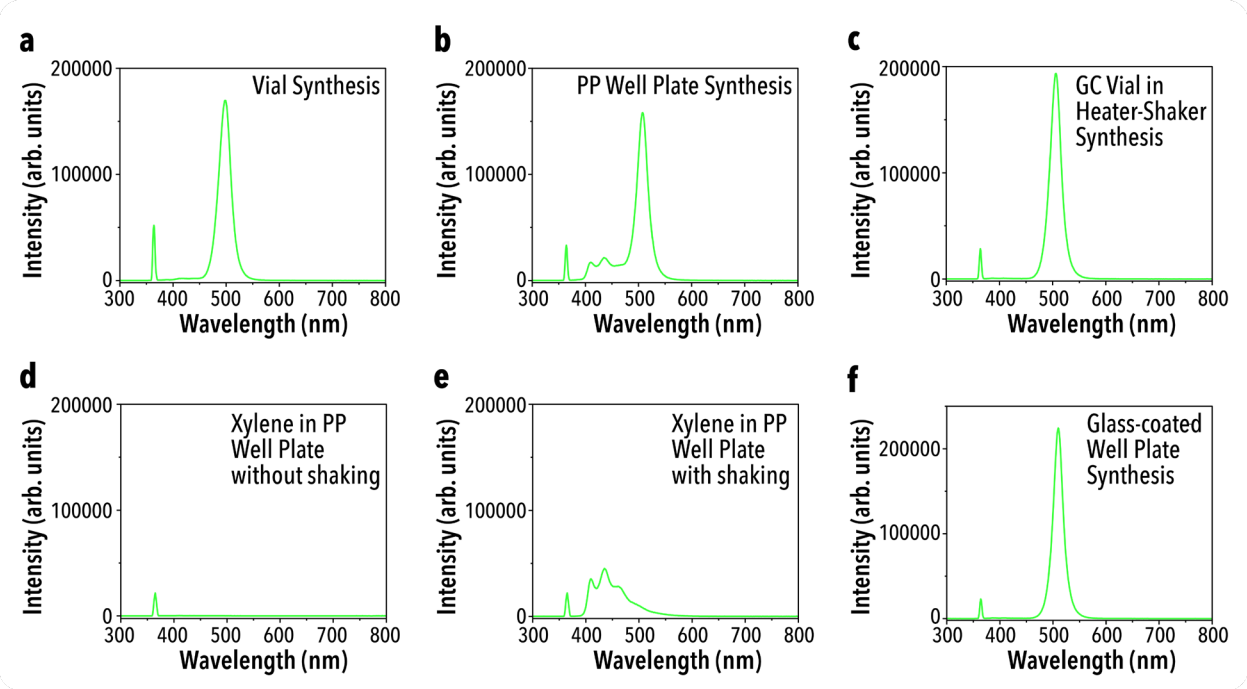

Fig. S1. *Benchmarking of different reactors for metal halide perovskite (MHP) nanocrystal (NC) synthesis. The emission spectra of MHP NCs synthesized using the same precursors and synthesis conditions in a (a) glass vial, (b) polypropylene (PP) well plate, (c) 1mL gas chromatography (GC) vial inserted in the PP well plate, (d) o-xylene in PP well plate without shaking; (e) o-xylene shaking in PP well plate, (f) glass-coated well plate. Secondary emission peaks at ~410 nm and ~440 nm are observed in reaction products using the PP well plate and not in the reaction product using a glass vial. In contrast of the flat signal from the o-xylene in PP well plate without shaking, the observation of the minor peaks from o-xylene shaking in PP well plate confirmed the minor peaks are stemmed from partially dissolved PP fragments in o-xylene. Replacing the PP well plate with a glass-coated well plate results in a similar reaction product to a glass vial.*

Fig. S2.

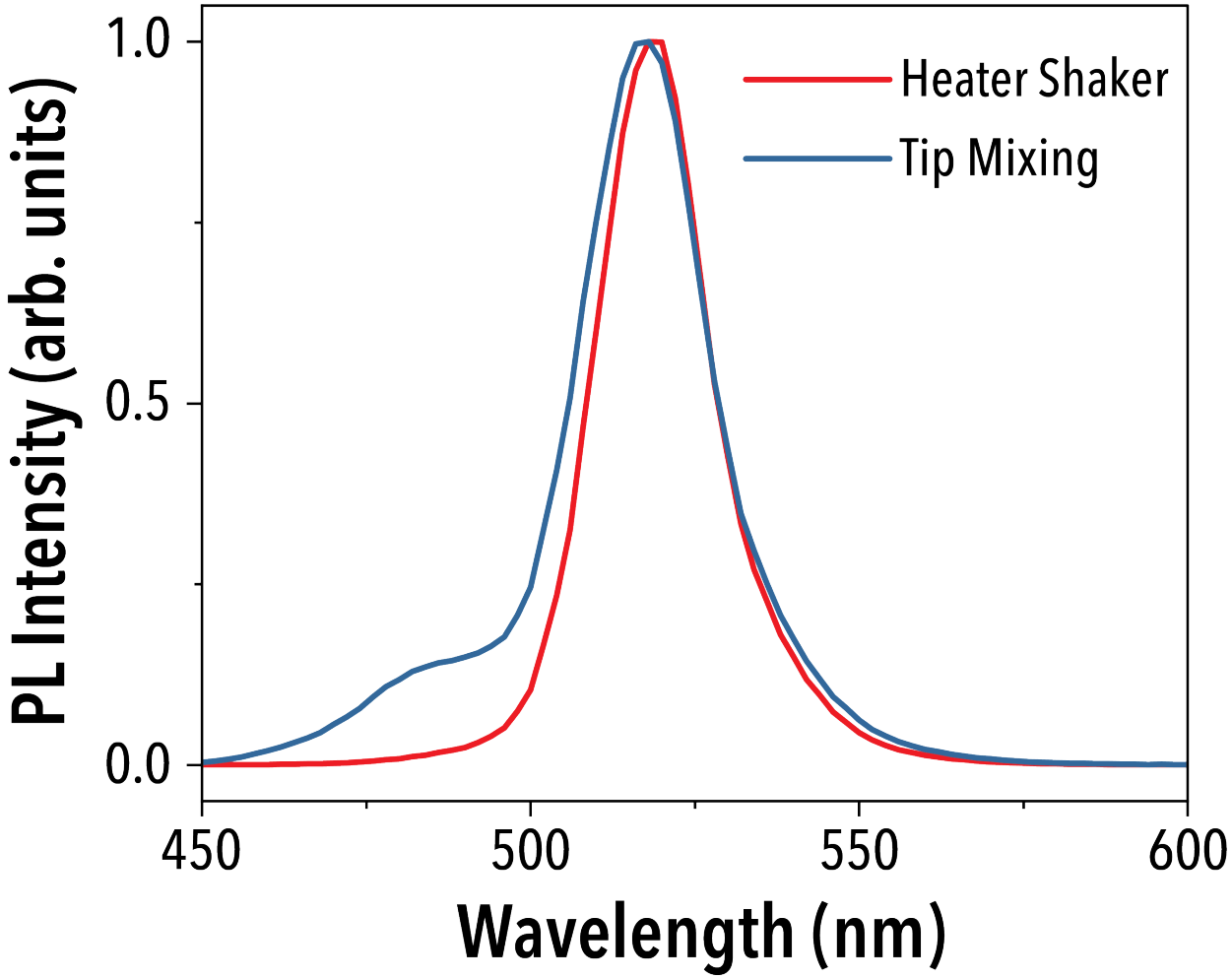

Fig. S2. *The comparison between precursor mixing within Rainbow's formulation and synthesis robot using a heater-shaker vs. a re-aspiration/dispensing via pipette tips. The heater-shaker mixing strategy provides single emission peak, indicating formation of a monodisperse metal halide perovskite (MHP) nanocrystals (NCs). In contrast, the tip mixing results in a secondary, blue-shifted emission peak, suggesting a polydisperse NC synthesis.*

Fig. S3.

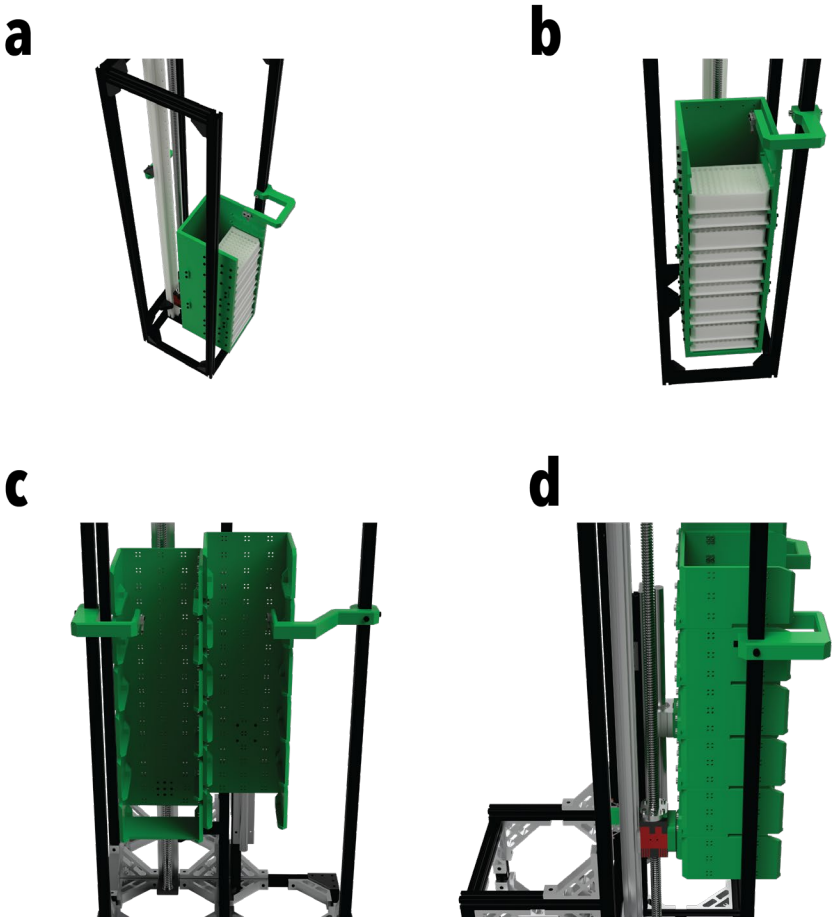

Fig. S3. *Illustration of the developed bespoke plate-feeder module. Rendered images of the well plate feeder from (a) side and (b) front views. Rendered images of the tip rack feeder from (c) front and (d) side views.*

Fig. S4.

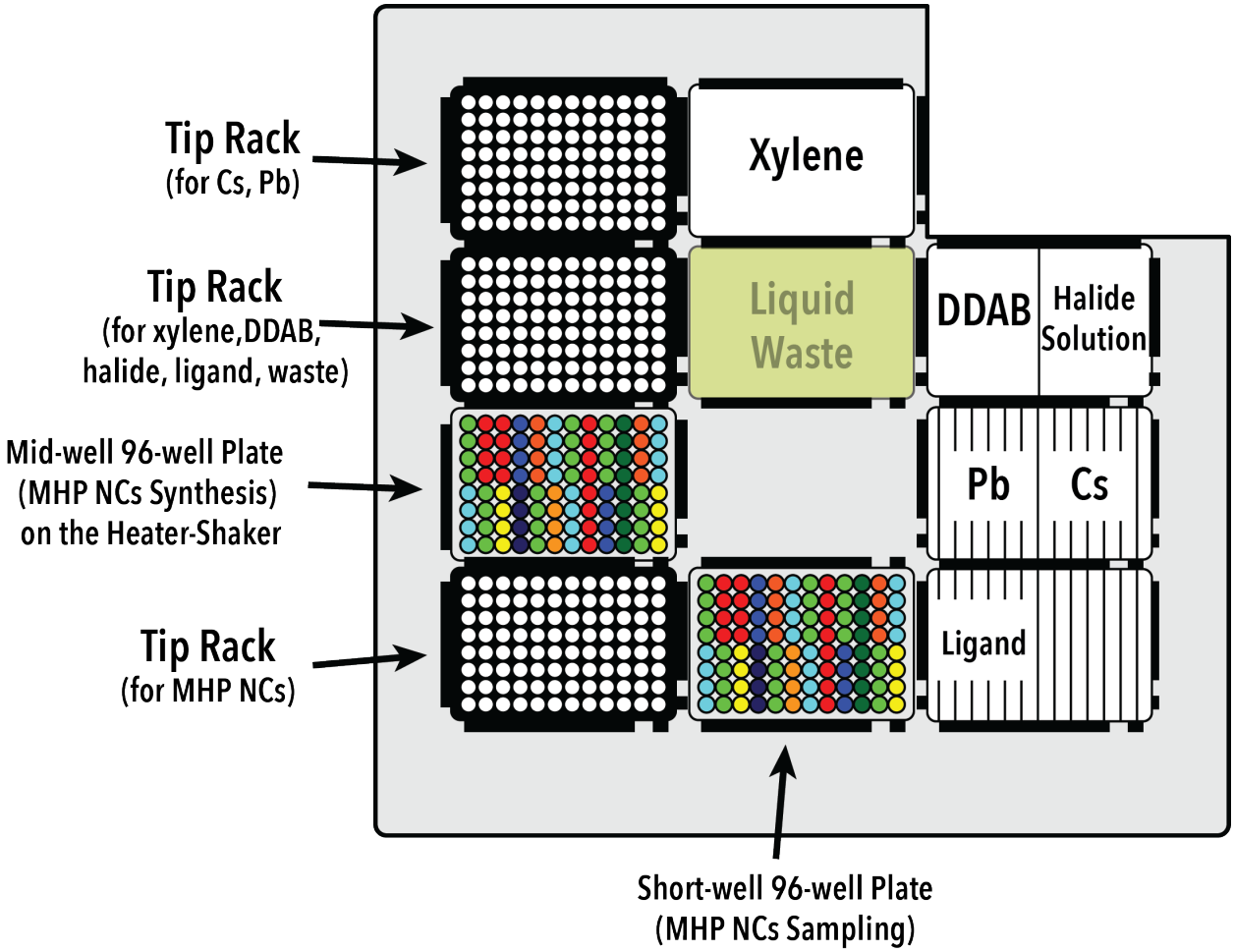

Fig. S4. *Illustration of the pipetting robot precursor allocation strategy. The Cs, Pb, and ligand precursors for each individual organic acid are stored in a designated channel (well), preventing cross-contamination of the precursors.*

Fig. S5.

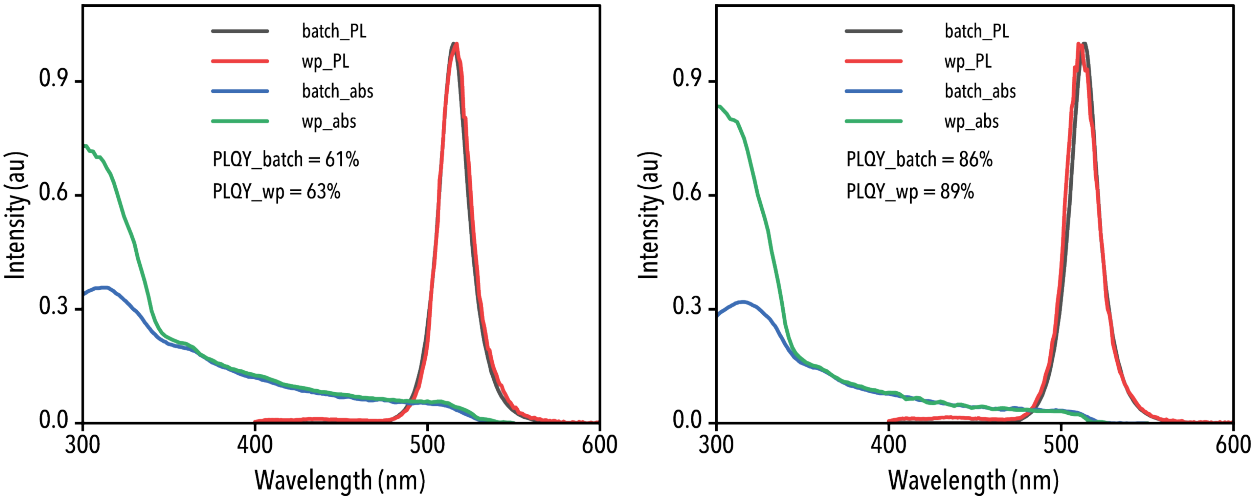

Fig. S5. *Rainbow's knowledge transferability and reliability. Comparison of manually synthesized metal halide perovskite (MHP) nanocrystals (NCs) in a glass vial characterized using a benchtop high-resolution spectrometer (Edinburgh Instruments, FS5 benchtop spectrometer) vs. automatically synthesized and characterized MHP NCs using the same precursors and synthesis conditions by Rainbow in a well plate. The agreement between the absorption and emission spectra of two different MHP NCs demonstrate the knowledge transferability and reliability of Rainbow's hardware.*

Fig. S6.

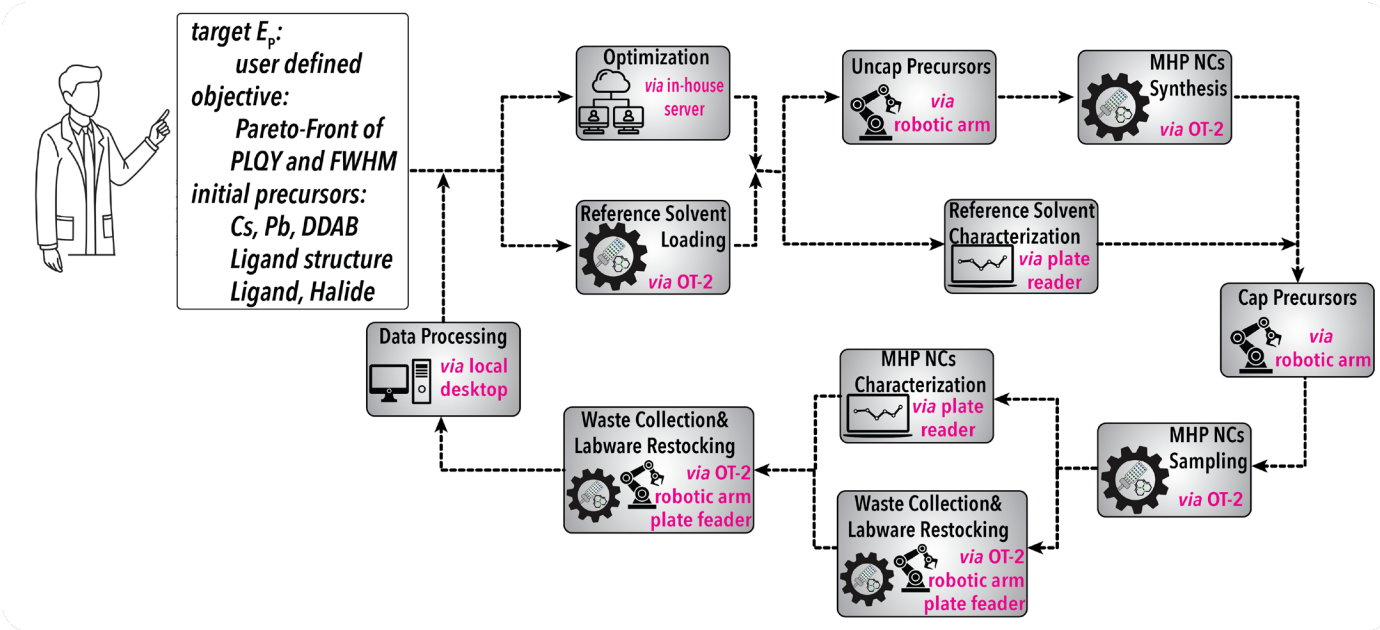

Fig. S6. *Rainbow's parallelized closed-loop workflow with the task and executing hardware module corresponding to each individual step.*

Fig. S7.

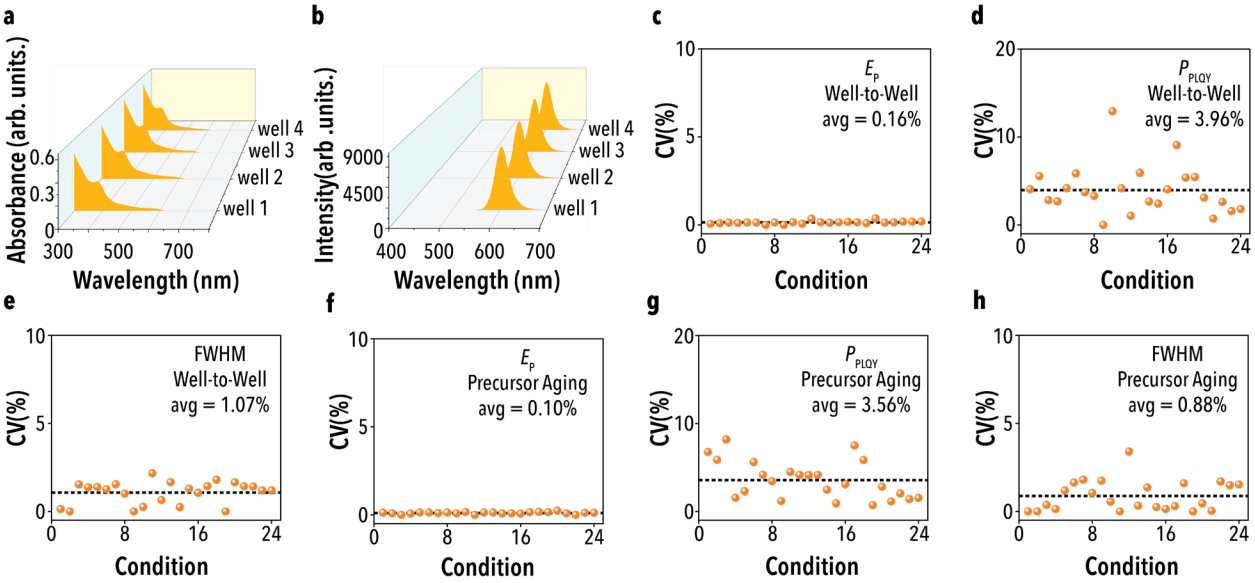

Fig. S7. *Reproducibility of Rainbow's workflow. Ultraviolet-visible (UV-Vis) (a) absorption and (b) emission spectra of the 4 reactor wells with a single experimental condition; the plate-average coefficient of variance (CV) corresponding to (c) peak emission energy (E_P), (d) proxy photoluminescence quantum yield (P_{PLQY}), and (e) full-width-at-half-maximum (FWHM) for a single iteration; the CV of (f) E_P, (g) P_{PLQY}, and (h) FWHM for the 10-h continuous experiments with the same set of experimental condition. The low CV values demonstrate the reproducibility of Rainbow's workflow. A relatively higher CV of P_{PLQY} is due to the influence from the variation of both the absorbance at excitation and emission intensity.*

Fig. S8.

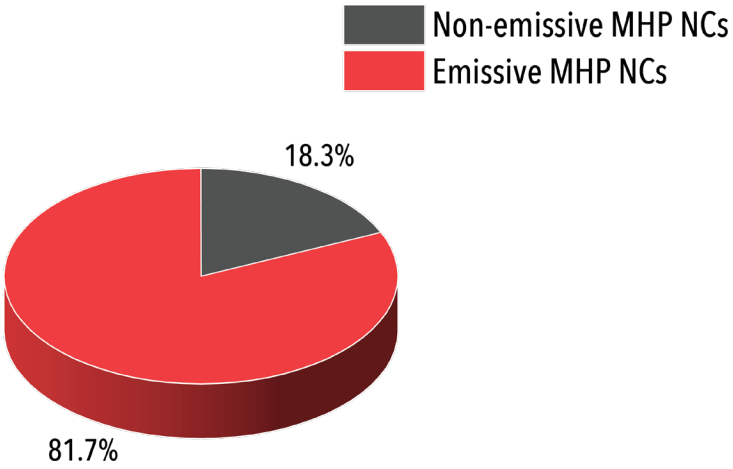

Fig. S8. *The percentages of the emissive (red) and non-emissive (black) metal halide perovskite (MHP) nanocrystal (NC) syntheses in a 5-iteration initialization experiments generated by Latin hypercube sampling. The same dataset is also used to initialize the classifier model.*

Fig. S9.

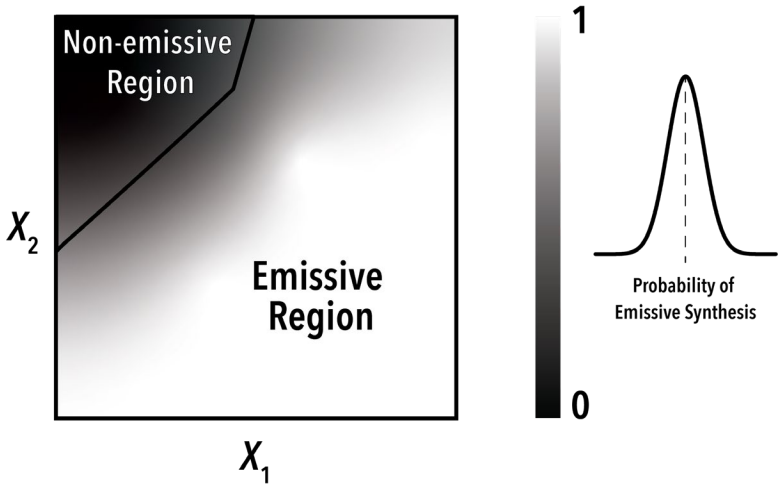

Fig. S9. *An illustration of the classifier model. The classifier model is a Gaussian process regression (GPR) predicting the probability of emissive synthesis for a given experimental condition denoted as X_1 and X_2. Either a lower level of X_2 or a higher level of X_1 can increase the emissive MHP NC synthesis success, while the region with lower level of X_1 and higher level of X_2 probably decrease the emissive MHP NC synthesis success.*

Fig. S10.

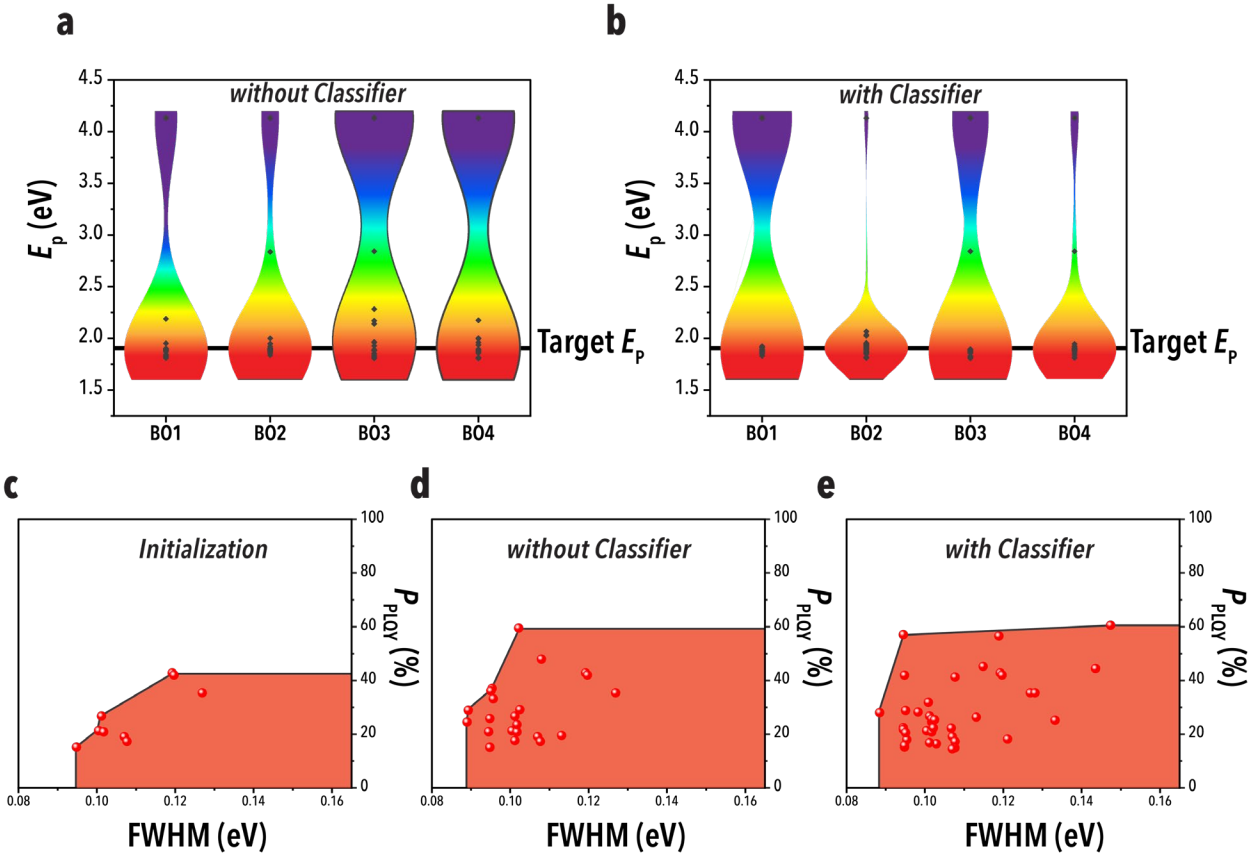

Fig. S10. *Experimental benchmarking of the classifier model. 4 cycles of Bayesian Optimization (BO) for a target peak emission energy (E_P) of 1.9 eV are implemented by Rainbow. The distribution of E_P of MHP NCs at each cycle of BO (a) without and (b) with the classifier. The BO cycles without the classifier start with high emissive rate in the first 2 cycles while lead to a higher non-emissive MHP NC synthesis (indicated by E_P ~4 eV, which is the artificially assigned impossible value for the identified non-emissive synthesis). In contrast, BO cycles with updating the classifier maintain a high emissive synthesis rate with fewer E_P ~4 eV. The full-width-at-half-maximum (FWHM) vs. proxy photoluminescence quantum yield (P_{PLQY}) Pareto-Front at the target E_P (c) by initialization experiments, (d) by initialization and 4 cycles BO without the classifier, and (e) by initialization and 4 cycles BO with the classifier. The random initialization only obtains a few points at the target E_P, with moderate FWHM and P_{PLQY}. The BO cycles without the classifier obtain several points at the target E_P with higher P_{PLQY} and lower FWHM, resulting in a larger Pareto-Front and increased hypervolume. The BO cycles with the classifier provide higher number of data points at the target E_P with higher P_{PLQY} and lower FHWM, offering an enlarged Pareto-Front and a larger hypervolume than BO cycles without the classifier.*

Fig. S11.

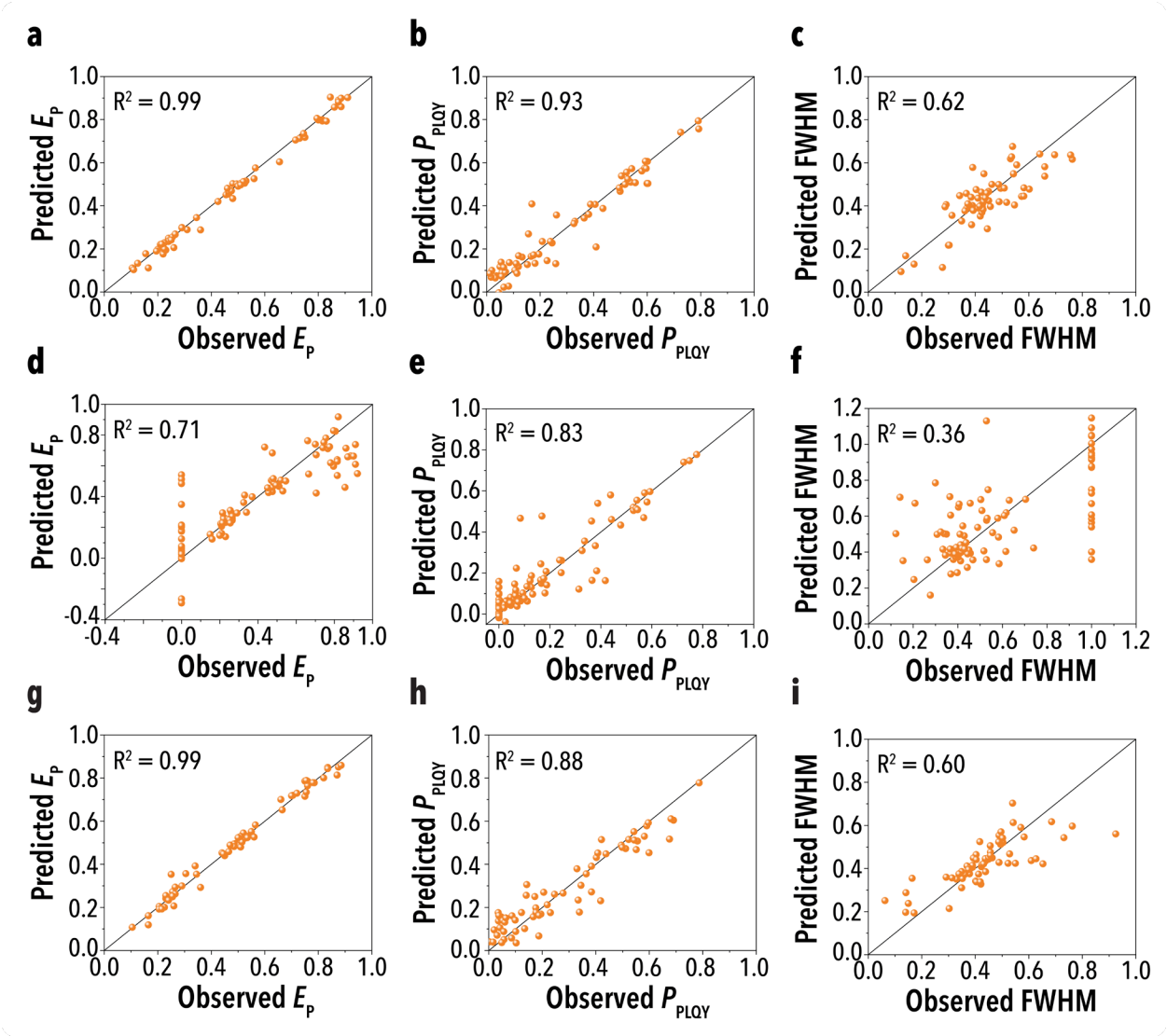

Fig. S11. *The Rainbow's digital twin prediction accuracy on the normalized test dataset. The parity plots illustrate the digital twin's (trained with only emissive data, using radial basis function (RBF) kernel for continuous variables) predicted values vs. the experimental data for (a) peak emission energy (E_P), (b) proxy photoluminescence quantum yield (P_{PLQY}), (c) full-width-at-half-maximum (FWHM); the digital twin's (trained with both emissive and non-emissive data, using RBF kernel for continuous variables) predicted values vs. the experimental data for (d) E_P, (e) P_{PLQY}, (f)FWHM, and the digital twin's(trained with both emissive and non-emissive data, using Matérn kernel for continuous variables) predicted values vs. the experimental data for (g) E_P, (h) P_{PLQY}, (i)FWHM.*

Fig. S12.

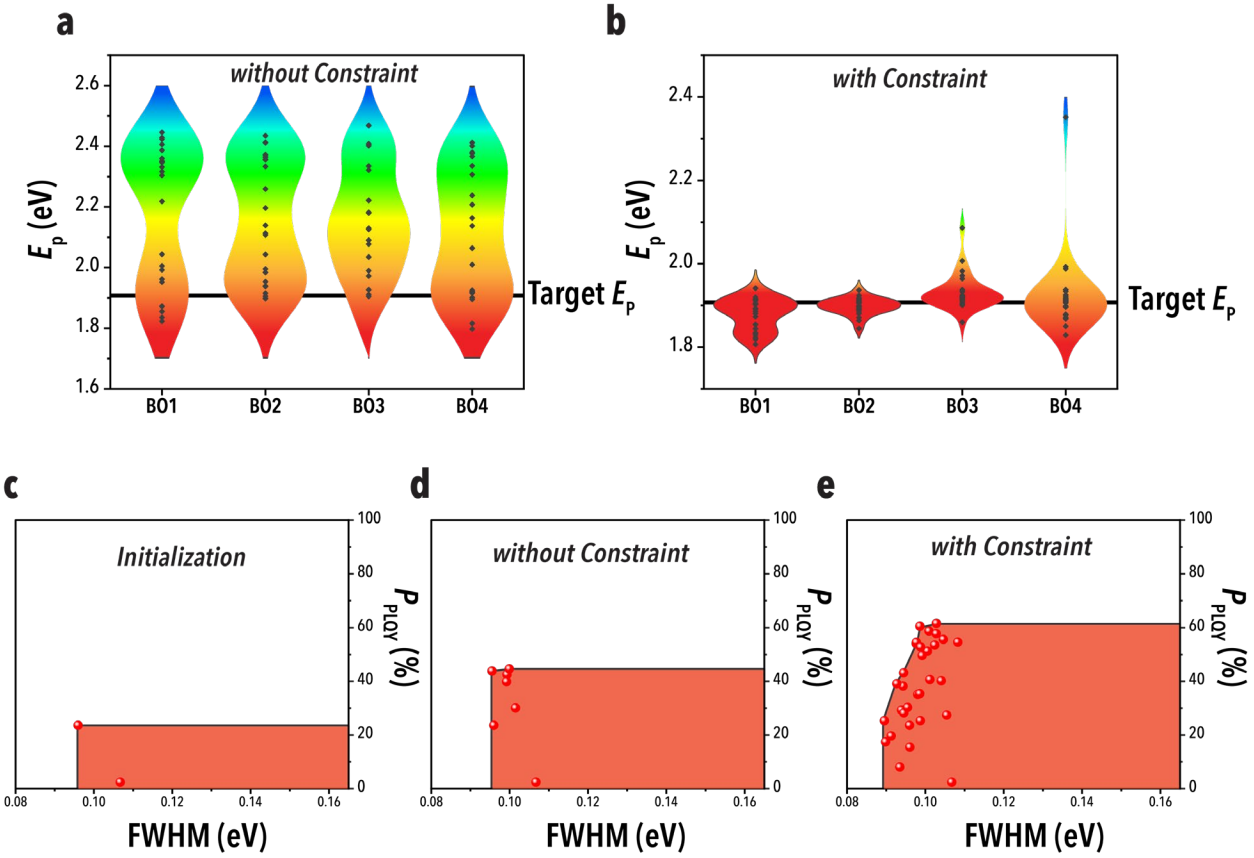

Fig. S12. *Virtual benchmarking of the constrained 4 cycles of Bayesian Optimization (BO) for a target peak emission energy (E_P) of 1.9 eV are conducted using Rainbow's digital twin. The distribution of E_P of metal halide perovskite (MHP) nanocrystals (NCs) at each cycle of BO (a) without and (b) with the constraint. The BO cycles without the constraint sample across the entire E_P range to maximize the expected hypervolume improvement (EHVI), thereby lowering the sampling efficiency. However, the BO cycles with the constraint explore the experimental conditions resulting in NCs with target E_P, providing a focused E_P distribution close to the target E_P. The full-width-at-half-maximum (FWHH) vs. proxy photoluminescence quantum yield (P_{PLQY}) Pareto-Front at the target E_P (c) by initialization experiments, (d) by initialization and 4 cycles BO without the constraint, and (e) by initialization and 4 cycles BO with the constraint. The random initialization only obtains a few points at the target E_P, with small hypervolume. The BO cycles without the constraint obtain a few points at the target E_P with higher P_{PLQY} and lower FWHM, resulting an enlarged Pareto-Front and increased hypervolume. The BO cycles with the constraint obtain higher number of data points at the target E_P with higher P_{PLQY} and lower FHWM, offering an enlarged Pareto-Front and a larger hypervolume than BO cycles without the classifier.*

Fig. S13.

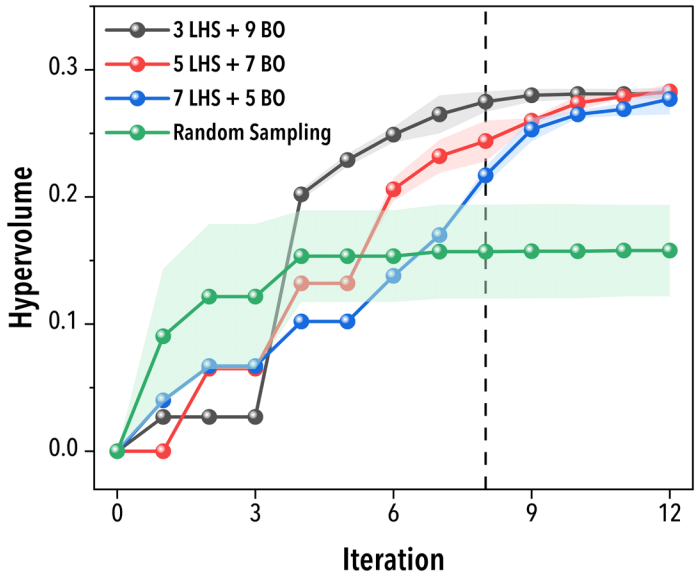

Fig. S13. *Rainbow's sample allocation study between surrogate model initialization and autonomous experimentation campaigns. With the fixed total experimental budget of 12 cycles, the hypervolume evolutions of 3 (black), 5 (red), and 7 (blue) initialization cycles vs. random sampling (green). With plenty of experimental cycles (12), the Latin hypercube sampling (LHS) initialization followed by Bayesian Optimization (BO) experiments converge to almost the same hypervolume, suggesting the efficient exploration of the chemical space and identification of the global optimum. 3LHS initialization followed by 5 BO cycles (dash line) can reach the converged hypervolume without spending the extra experimental budget. Random sampling cycles achieve only ~half of the hypervolume identified by the LHS + BO.*

Fig. S14.

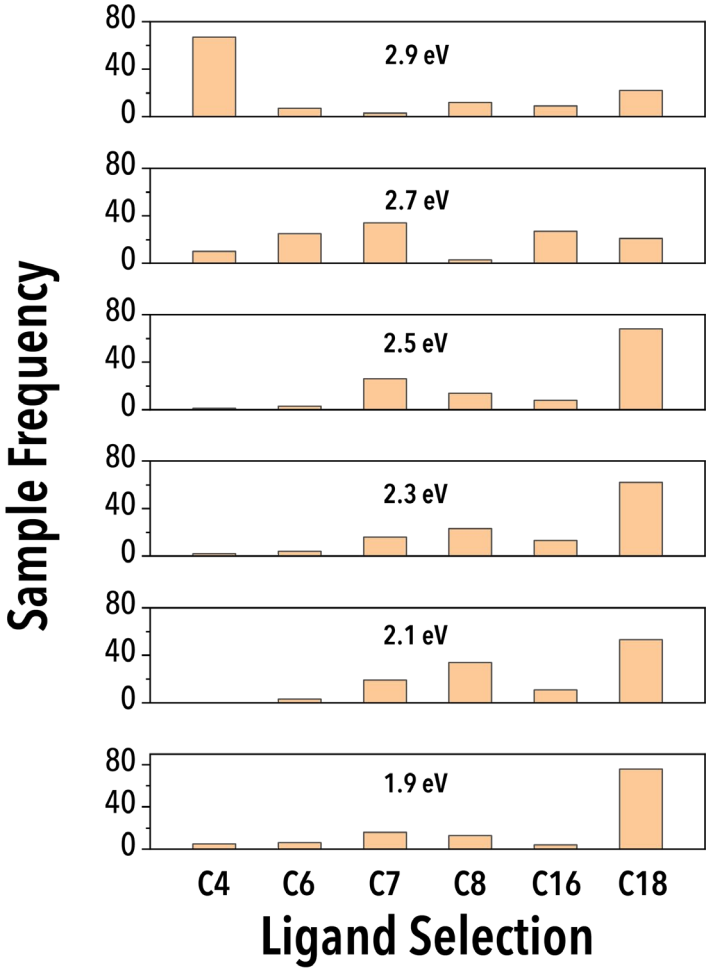

Fig. S14. *Organic acid ligand selection among butyric acid (C4), hexanoic acid (C6), heptanoic acid C7), octanoic acid (C8), 2-hexyldecanoic acid (C16) and oleic acid (C18) by Rainbow's AI agent for different target peak emission energy (E_P). C18 is heavily sampled for 1.9 -2.5 eV campaigns. C7 is highly suggested for 2.7 eV campaign and C4 is the mostly recommended ligand for 2.9 eV campaign. With the increasing target E_P, the alkyl chain length of the recommended organic acid ligand becomes shorter.*

Fig. S15.

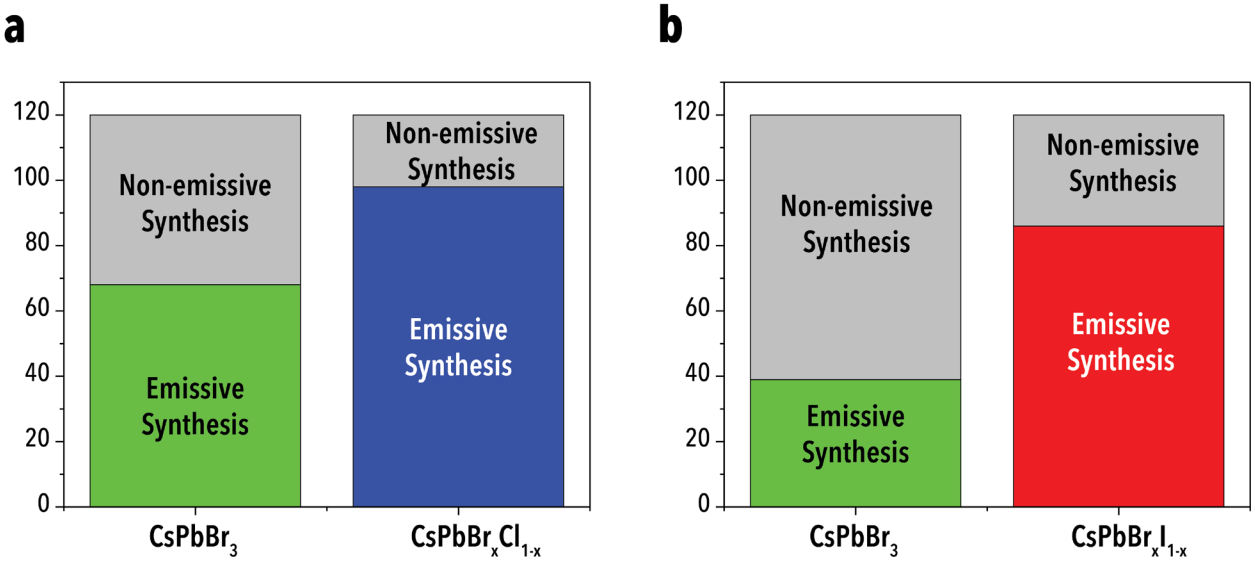

Fig. S15. *The influence of halide exchange reaction on the metal halide perovskite (MHP) nanocrystals' (NCs') colloidal stability. The successful (green, blue, or red) and unsuccessful (grey) synthesis before and after halide exchange reaction of (a) 2.9 eV campaign and (b) 1.9 eV campaign. The success rate is improved after halide exchange reaction, demonstrating the enhanced NC colloidal stability.*

Fig. S16.

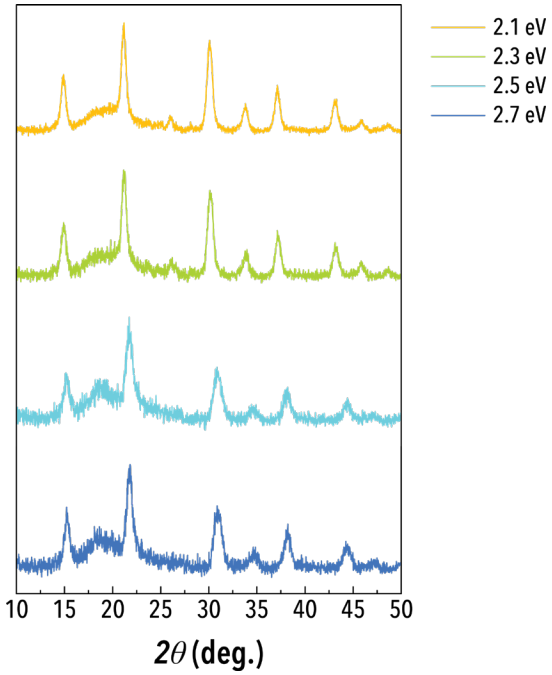

Fig. S16. *Grazing incidence X-ray diffraction patterns for the best-performing metal halide perovskite (MHP) nanocrystals (NCs) with selected target peak emission energies (E_{PS}). The best-performing MHP NC for every target E_P is identified as the NC with the highest proxy photoluminescence quantum yield (P_{PLQY}) with the full-width-at-half-maximum (FWHM) below 0.11 eV, which is considered as a uniform NC size distribution.*

Fig. S17.

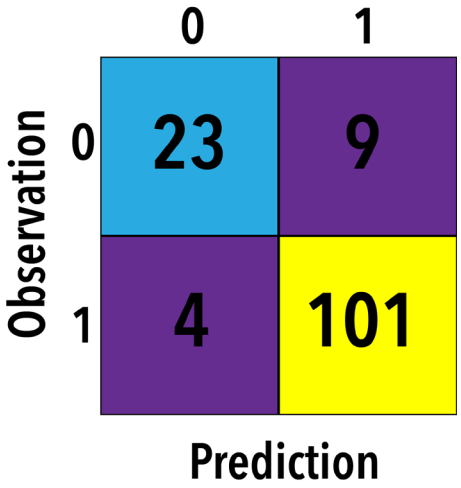

Fig. S17. *The confusion matrix of the trained classifier's prediction on the test dataset.*

Fig. S18.

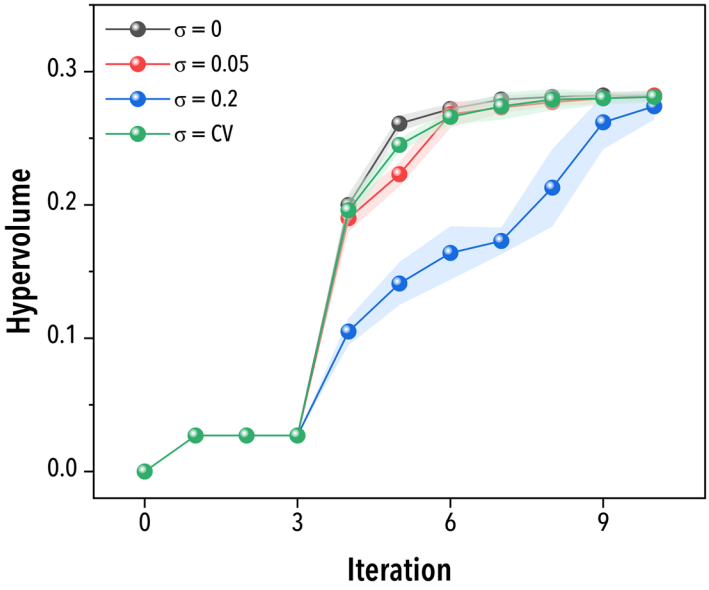

Fig. S18. *The hypervolume evolutions obtained from virtual Bayesian Optimization (BO) benchmarking campaigns with multiple noise levels. With increased uncertainty level tested, the hypervolume converged slower while still reached the similar convergence after 7 cycles of virtual BO simulations, confirming the robustness of Rainbow's BO framework against uncertainties.*

Fig. S19.

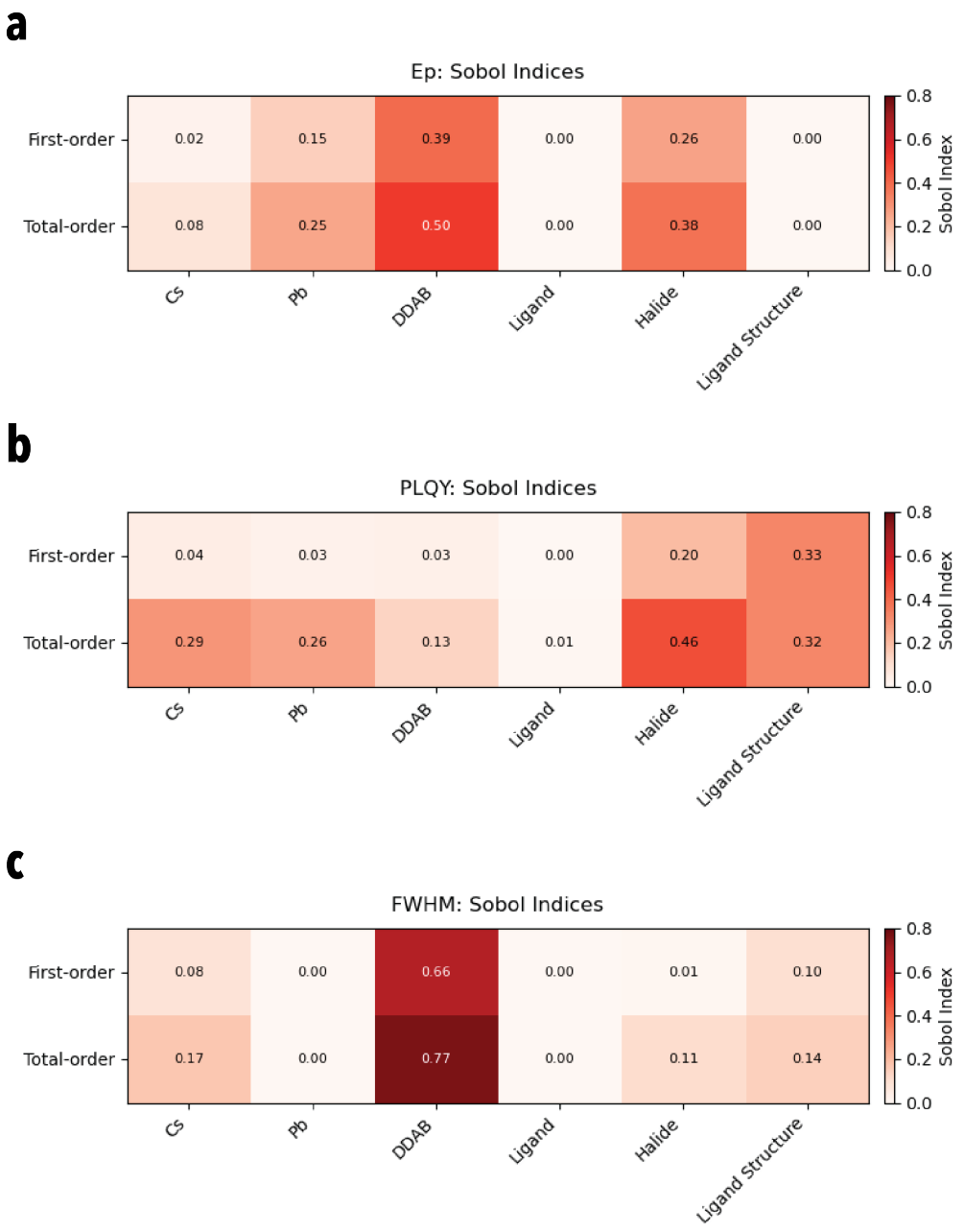

Fig. S19*. Sobol indices-based sensitivity analysis for input parameters' contribution on the variance of (a) peak emission energy (E_P), (b) proxy photoluminescence quantum yield (P_{PLQY}), and (c) full-width-at-half-maximum (FWHM).*

Fig. S20.

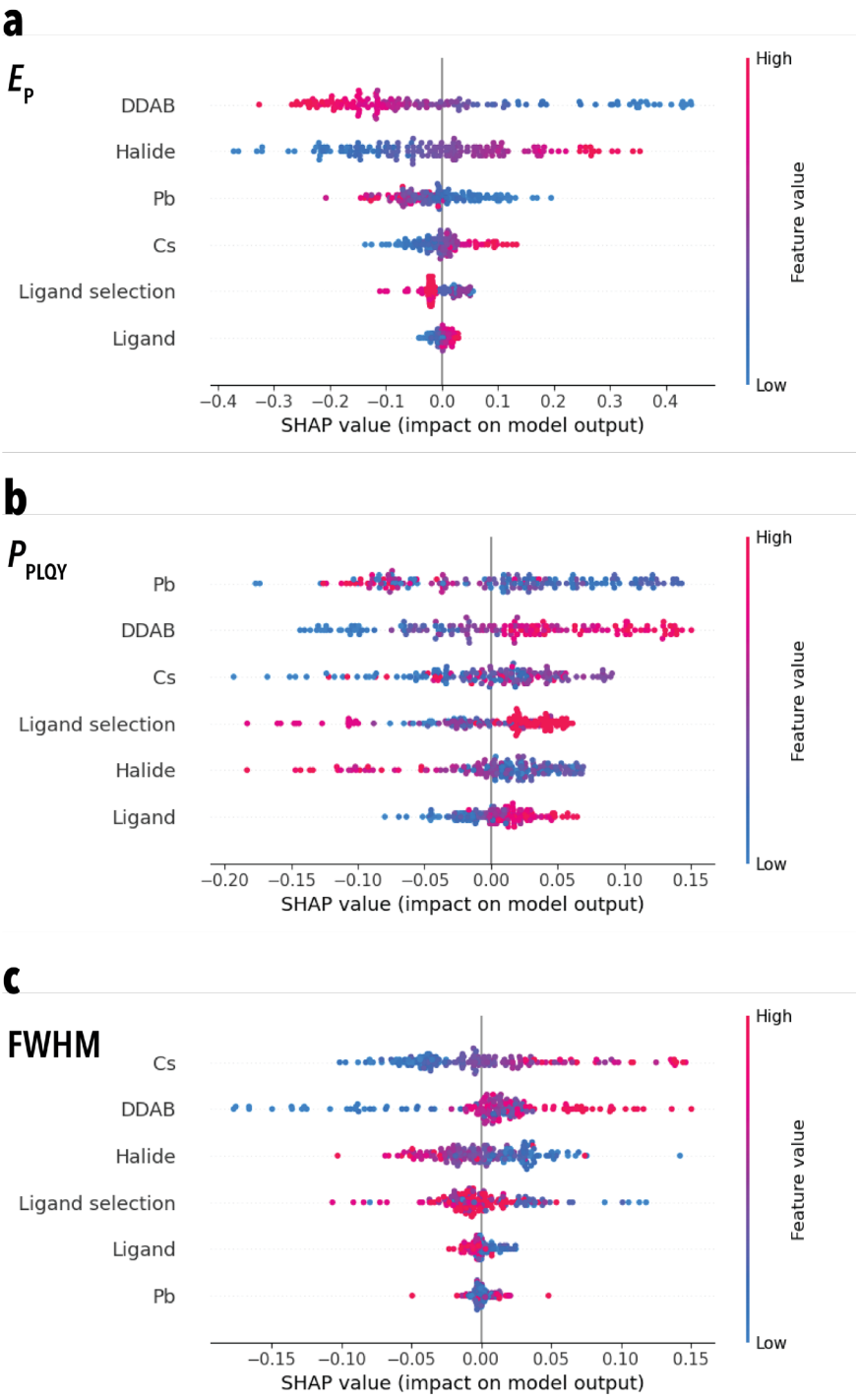

Fig. S20*. Shapley analysis for input parameters' contribution on the model prediction of (a) peak emission energy (E_P), (b) proxy photoluminescence quantum yield (P_{PLQY}), and (c) full-width-at-half-maximum (FWHM).*

Fig. S21.

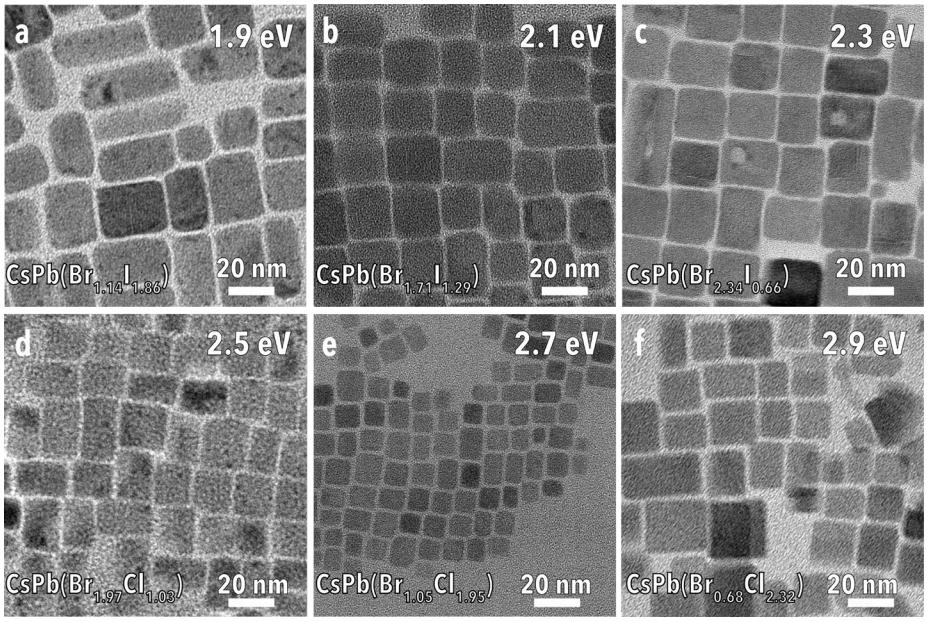

Fig. S21. *TEM images and estimated chemical composition of the scaled-up synthesis of best-performing metal halide perovskite (MHP) nanocrystals (NCs) for target peak emission energy (E_P) at (a) 1.9 eV; (b) 2.1 eV; (c) 2.3 eV; (d) 2.5 eV; (e) 2.7 eV; (f) 2.9 eV. The chemical compositions are estimated by analysis of energy-disperse X-ray spectroscopy.*

Table S1. *Variable type and boundaries or choices for input parameters*

variable	**Cs (μL)**	**Pb (μL)**	**DDAB (μL)**	**ligand (μL)**	**halide (μL)**	**ligand structure**
type	continuous	continuous	continuous	continuous	continuous	discrete
lower bound	20	20	20	20	20	[C4, C6, C7, C8, C16, C18]
upper bound	300	300	300	100	300	

Table S2. *Variable type and boundaries for output parameters*

variable	**absorbance (arb. units.)**	E_P **(eV)**	P_{PLQY} **(%)**	**FWHM (eV)**
type	continuous	continuous	continuous	continuous
lower bound	0	1.8	0	0.08
upper bound	1	3.1	100	0.16